DIFFRACTION IMAGING USING SPECULARITY GATHERS

I. STURZU[1], A.M. POPOVICI[1] and T.J. MOSER[2]

[1] *Z-Terra Inc., 17171 Park Row, Houston, TX 77084, U.S.A. isturzu@z-terra.com*
[2] *Moser Geophysical Services, van Ikemadelaan 550A, 2597 AV The Hague, The Netherlands.*

(Received May 30, 2013; revised version accepted November 2, 2013)

ABSTRACT

Sturzu, I., Popovici, A.M. and Moser, T.J., 2014. Diffraction imaging using specularity gathers. *Journal of Seismic Exploration*, 23: 1-18.

The separate imaging of subsurface diffractors is a key ingredient in the development of high-resolution imaging technologies. We here produce images of diffractors using depth migration algorithms modified to attenuate the energy from specular reflectors. The seismic events from a pre-stack seismic dataset are migrated to proper depth and location using the final velocity model obtained by the velocity model building process, but the output is assigned to separate bins according to the value of a specific parameter called specularity. The specularity gathers are post-processed using a plane wave destructor filter to attenuate the contribution coming from specular reflectors. The method is demonstrated on two synthetic models and on a field data target in the Teapot Dome reservoir.

KEY WORDS: seismic migration, diffraction imaging, high-resolution imaging, plane wave destructor, common image gather, specularity gather.

INTRODUCTION

High-resolution imaging of the small scale fractures in reservoirs improves production and recovery efficiency, reduces field development cost, and decreases the environmental impact of developing the field by using fewer wells to optimally produce the reservoir. Deploying this technology is a fundamental advance in high-resolution 3D prestack data imaging of complex geological structures. Current diffraction imaging research has identified a new approach to image small scale faults, pinch-outs, salt flanks, reflector unconformities, and, in general, any small scattering objects by using diffraction imaging as a complement to the structural images produced by reflection imaging (Shtivelman and Keydar, 2004; Khaidukov et al., 2004; Taner et al., 2006; Fomel et al., 2006; Moser and Howard, 2008; Moser, 2009; Klokov et al., 2010; Klokov et al., 2011; Dell and Gajewski, 2011; Moser, 2011).

0963-0651/14/$5.00

The main goal of conventional depth seismic processing is to enhance specular reflections. Many time processing steps are designed to increase the lateral coherency of the reflections, from interpolation, FXY deconvolution and FK filtering, to wave-equation binning. Since diffractions have a different move-out than reflections, processing steps designed to enhance reflections result in attenuating diffractions. Seismic methods are generally limited in their resolving power to a fraction of the dominant wavelength at the target that in practical cases cannot be smaller than one quarter, as shown in Zeng (2009) and references therein. If layers are thinner than this value, tuning and multiple-reverberation effects make the stratigraphic interpretation of the images difficult and unreliable. Decreasing the wavelength of the seismic waves reflected at the target is nearly impossible because of the dissipative nature of the overburden that attenuates the high-frequencies in the seismic wave-field. Furthermore, the high frequencies that are present in the data are often lost during standard processing. High-resolution imaging is of value, for instance to enable identification of small scale faults and to locate formation pinch-outs. Standard approaches to obtain high-resolution information, such as coherency analysis and structure-oriented filters, derive attributes from stacked, migrated images. In comparison, diffraction imaging can act directly on the pre-stack data, and has the potential to focus and image super-resolution structural information as a consequence of the redundancy present in the pre-stack data.

THEORY AND METHOD

Diffractions are the seismic response of small elements (or diffractors) in the subsurface of the earth, such as small scale faults, near surface scattering objects, and, in general, all objects which are smaller than the seismic wavelength. Diffraction imaging uses diffractions to focus and image the structural elements that produced those diffraction events. Since diffractors are, by definition, smaller than the wavelength of seismic waves, diffraction imaging has the potential of providing super-resolution information, to image details that are beyond the classical Rayleigh limit of half a seismic wavelength. The importance of diffractions in high-resolution structural imaging has been emphasized in many recent publications (Shtivelman and Keydar, 2004; Khaidukov et al., 2004; Taner et al., 2006; Fomel et al., 2006; Moser and Howard, 2008; Moser, 2009; Klokov et al., 2010; Klokov et al., 2011; Dell and Gajewski, 2011; Koren and Ravve, 2011; Klokov and Fomel, 2012). Still, diffraction imaging is not widely used tool. In fact, most algorithms that are used to process seismic data explicitly enhance reflections and implicitly suppress diffracted energy. The goal of diffraction imaging is not to replace these traditional algorithms, but rather to provide an additional 3-D or 4-D volume containing information about diffractors that would be able to fill in the small, but potentially crucial, structural details.

A true diffraction image is not optimally obtained by post-processing a traditional seismic image even if the seismic image is obtained by an algorithm that does not suppress diffractions. While diffractors will appear in the image, usually in the form of discontinuities, they have much lower amplitudes than reflecting structures. On the other hand, by imaging diffractors using the pre-stack data, the diffractor amplitude can be enhanced while the specular reflections can be attenuated. Furthermore, apparent discontinuities in the seismic image can have a variety of causes other than diffractions, including small errors in the velocity model of the earth that was used to obtain the image, so the post-stack/post-processing approach would not be able to discriminate between discontinuities coming from diffractions and those coming from processing errors.

Techniques for diffraction imaging fall into two categories. In the first category are methods that separate the seismic data into two parts, one that contains the wave energy from reflections (specular energy) and the other that contains the wave energy from diffractions. Each component is used to provide an image through traditional seismic imaging methods. In the second category are methods that do not separate the input seismic data, but rather performs filtering during migration. Moser and Howard (2008) and Moser (2009) extracted the local direction of specularity from a previously obtained migration stack, and used this information during a subsequent migration step in order to filter the events that satisfied (to a given degree) Snell's law. Koren and Ravve (2011) pre-computed a directivity-dependent specularity attribute using information from the velocity model and the acquisition geometry and used angle domain gathers in order to suppress the specularity energy associated with horizontal events in the angle domain gathers. In this paper we follow the approach from Moser and Howard (2008). The parameters governing the specularity filtering are rather arbitrary, if no further investigation is implied. Sturzu et al. (2013) introduced a new concept - specularity gathers - that proved to be very useful in the design of proper parameters for the specularity filter. Below we show how we can selectively filter the specular energy within specularity gathers to obtain the diffraction images after stacking along the specularity dimension.

In Kirchhoff migration, energy is propagated to all possible reflection points in the model space. After all events on all traces are propagated, an image is generated by stacking (summing) all individual contributions. The propagation of the events usually uses Green's functions computed in the form of travel-time tables (the time of propagation from the source defined by the trace to the image point and further to the receiver defined by the trace.) Stacking reinforces in-phase energy corresponding to true reflectors and cancels out-of-phase energy that does not correspond to a true reflector. A conventional Kirchhoff migration forms a seismic image as:

$$V(\mathbf{x}) = \int dtdsdrU''(t,\mathbf{s},\mathbf{r})\delta[t - T(\mathbf{s},\mathbf{x},\mathbf{r})] \quad , \tag{1}$$

where δ is the Dirac delta function, $U''(t,\mathbf{s},\mathbf{r})$ the (second time derivative) pre-stack data, depending on time t and shot/receiver positions $\mathbf{s}/\mathbf{r}$, $T(\mathbf{s},\mathbf{x},\mathbf{r})$ is the travel time from $\mathbf{s}$ to $\mathbf{r}$ via the subsurface image point $\mathbf{x}$, computed by ray tracing in a given reference velocity model, and $V(\mathbf{x})$ the resulting migrated image. The sum is carried out over the time samples and all source and receiver pairs $(\mathbf{s},\mathbf{r})$, in the seismic data.

In the earth's subsurface the local discontinuities (reflectors) can be modeled either as surfaces, edges, or isolated tips or points. For a smooth surface reflector, the corresponding part of the image is a locally continuous, planar surface that generates specular events, meaning that they strictly obey Snell's law. Events backscattered from all other types of discontinuities are diffractive and do not obey Snell's law. Diffraction imaging attenuates the contribution of specular events in a migrated image.

In the final image stack, a specular element can be approximated locally as a planar surface, while the isochrone surfaces (computed using the travel-time tables) should be tangent to the planar surfaces corresponding to the specular elements, as a direct consequence of Snell's law. For diffractive events, however, there is no such constraint. For a given trace in the data and a point in the image (1), we define the *specularity* in terms of the specularity angle, defined by the normal to a locally planar structure (dominant at that image point) and the direction of the gradient of the total travel-time from the source to the receiver via the image point. We choose the absolute value of the cosine of the specularity angle as the actual value of specularity. This can be expressed mathematically as:

$$S(\mathbf{s},\mathbf{x},\mathbf{r}) = |\mathbf{n}\cdot T_x| / \| T_x \| \quad , \tag{2}$$

where T_x denotes the gradient of $T(\mathbf{s},\mathbf{x},\mathbf{r})$with respect to $\mathbf{x}$, and $\mathbf{n}$ is the unit vector normal to the reflector surface, also depending on $\mathbf{x}$, and the dot denotes the scalar product. If $\mathbf{x}$ is located on a strong reflector, the value of the specularity should be equal to unity, $S = 1$, because the two rays (coming from the source and that going toward the receiver) then obey Snell's Law with respect to the normal to the reflector $\mathbf{n}$, so the angle bisector of the two rays is aligned with the normal to the surface. In diffraction imaging framework, this is a pure specular reflection that has to be attenuated. If the angle bisector of the rays and the normal to the surface are not perfectly aligned, $S < 1$ and the energy is non-specularly scattered.

The concept of pure specularity as defined above has to be amended using the concept of the Fresnel zone, which is a frequency-dependent volume around

the ray within which most of the wave energy is interfering constructively and can be treated as a single arrival wave. All the points from a Fresnel zone have to be considered together, even if they have slightly sub-unitary values for specularity. That is why pure specularity has to be defined by a frequency-dependent interval close to unity. In Fig. 1, we illustrate this situation by comparing a pure specular reflection with a pure diffraction. The Fresnel zones are depicted by hatched areas.

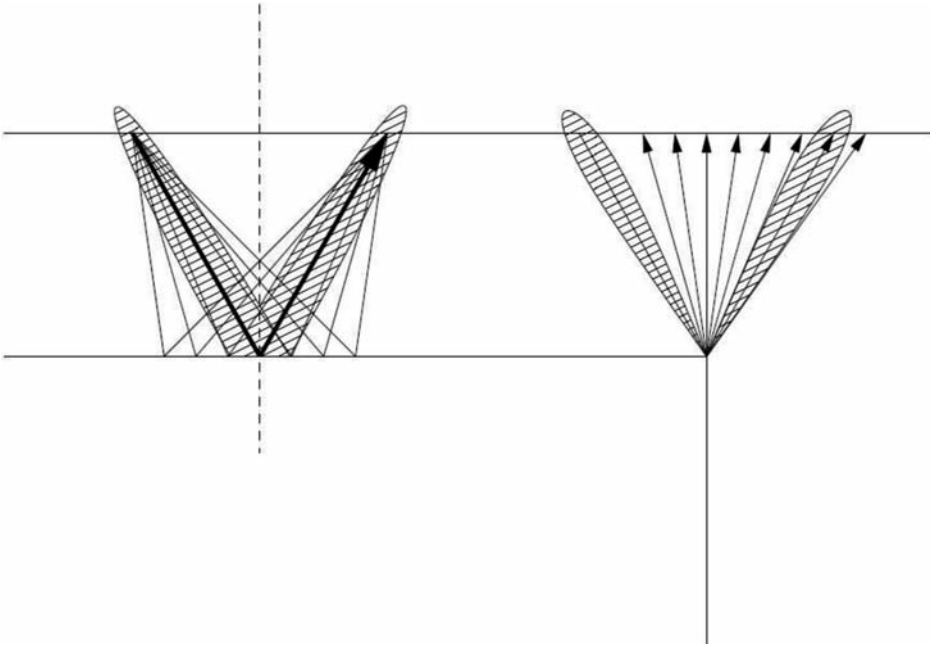

Fig. 1. Comparison between a pure specular reflection and a pure diffraction case. The Fresnel zone for the reflection are depicted by the hatched areas.

A straightforward procedure for obtaining a diffraction image is outlined in Moser and Howard (2008) and Moser (2009). First, using pre-stack Kirchhoff migration, we obtain the seismic image; this image will include both reflections and diffractions, but the reflections dominate the image. The second step is to analyze the structures in the Kirchhoff image and determine the normal vector to these structures at each image point. Using a migration stack to obtain this information, rather than to extract it from the final velocity model, is critical in cases when the stratigraphic non-conformity is important (Moser, 2009). The second step has to be performed on an optimally focused image, obtained using the best velocity model, so that the information extracted is related to the geological geometry of the undersurface. In a subsequent migration run, the migrated seismic events are stacked using a weight designed in order to attenuate the contribution of the specular events (specularity value close to 1).

An important challenge comes from the fact that there is no a priori procedure to define the limits of the pure specularity region as a function of specularity itself, so one cannot design a proper weighting function before the last migration run. A simple trial-and-error method can be too computationally demanding. Specularity gathers, a novel technique introduced in Sturzu et al. (2013) can be used to increase the efficiency and accuracy of the diffraction imaging technique. A specularity gather is similar to an offset or angle common image gather, in which the migrated seismic events are separated according to the value of specularity rather than of the offset or, respectively, reflection angle. The events are migrated to the proper depth and are partially stacked according to the specularity values in pre-defined specularity bins. The specularity gather can be formally written as:

$$V_{sg}(\mathbf{x},S) = \int \mathrm{d}t\mathrm{d}s\mathrm{d}r U''(t,\mathbf{s},\mathbf{r})\delta[t - T(\mathbf{s},\mathbf{x},\mathbf{r})]\delta(S - |\mathbf{n}\cdot T_x|/\|T_x\|) \quad . \quad (3)$$

In a post-processing technique similar to the muting of the offset gathers, the diffraction image can be obtained after a weighted stack over all the specularity values:

$$V_d(\mathbf{x}) = \int_0^1 \mathrm{d}S\, w(\mathbf{x},S) V_{sg}(\mathbf{x},S) \quad . \quad (4)$$

The use of specularity gathers has the advantage that the weighting function is designed after migration and therefore is constructed, and updated, very efficiently. In particular, the weighting function can be spatially variable [$w = w(\mathbf{x},S)$] and adapted to the local Fresnel zone width, which is difficult to estimate a priori, but becomes feasible using specularity gathers. Also, feedback from interpretation can be easily included in the weighting function, and hence in the final diffraction image.

As shown in Sturzu et al. (2013), for a correct velocity model and in the ideal infinite-frequency limit, a specular reflection event appears in the specularity gathers as a focused spot on the $S=1$-axis. Point diffractions appear as flat events extending over $0 < S < 1$. Edge diffractions in three dimensions appear as dipping events, as they obey Snell's law only along the edge, but not transversely to it (Moser, 2011). For finite bandwidth seismic responses, the situation is slightly different. Specular reflections also appear as dipping events, as the non-specular part of reflected energy outside the Fresnel zone is not related to the shortest reflection path following Fermat's principle.

In a Common Image Point section of the specularity gather, the image is obtained from different portions of the isochrones of different traces. For example, in the case of a horizontal flat reflector with a constant velocity

overburden, the isochrones are ellipses. The specularity angle in each point of the ellipse is monotonically changing from zero below the Common Image Point to 90 degrees at zero depth. In a Common Image Point section of the specularity gather, the bin for the maximum specularity (specularity angle close to zero) is formed by pieces of the ellipses corresponding to maximum depth. Here, traces with any offset should contribute. The very next specularity bin (in the same Common Image Point section) is formed by the contributions of the traces with neighboring mid-points, but having the right offset to yield the designed value of the specularity. The location of the events should be shallower than the location of the event in the previous bin. This interpretation pattern can be applied to subsequent specularity bins, ending with the bin for zero specularity, which has to have contributions only at zero depth, but from all traces.

Fig. 2 shows migration results for the case of a horizontal flat reflector with a constant velocity overburden. The sub-figures depict: (a) a Common Image Point (or vertical) section from the specularity gather (a partial image obtained for a given vertical in the image space and all values of the specularity), (b) the final stack over all values of specularity, equivalent to the standard migrated image, and, in each of panels (c), (d) and (e) a specularity section (a partial image obtained for a given value of the specularity for all points in the image space) for S = 1.0, S = 0.9 and S = 0.8, respectively. Sub-Figs. 2(d) and 2(e) contain out of Fresnel zone ghosts for the main specular event depicted in sub-Figs. 2(b) and 2(c). Remarkably, stacking over all values of specularity is able to fully cancel the contribution of all the ghosts in the final

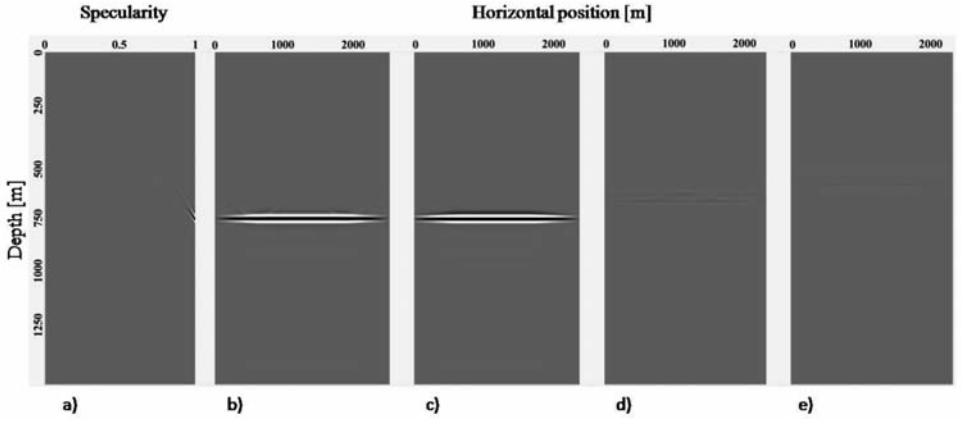

Fig. 2. Migration results for a horizontal flat reflector with a constant velocity overburden: (a) the specularity gather for the horizontal position at x = 1250 m; (b) The stack over all values of specularity, equivalent to a standard migrated image; (c) specularity section for S = 1.0; (d) specularity section for S = 0.9; (e) specularity section for S = 0.8.

stack (b). Fig. 3 show similar results for a point diffractor in a constant velocity medium. In the left panels is displayed the migration image, obtained by stacking along all specularity values in the specularity gather. The specularity gather in the exact location of the point diffractor is a flat horizontal event (sub-figure 3(a) central panel); when moving slightly away from this point, the horizontal event splits into two (sub-Fig. 3(b) central panel). The right panels show two specularity sections, for S = 1.0 in sub-Fig. 3(a) and for S = 0.8 in sub-Fig. 3(b).

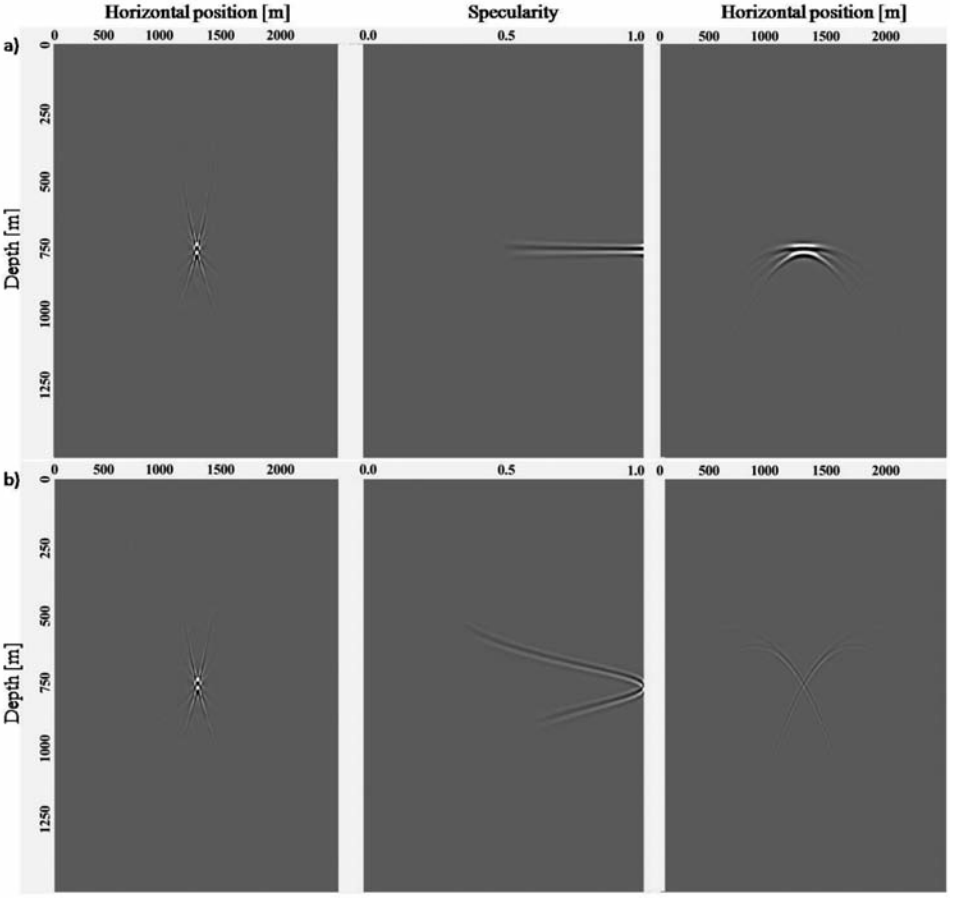

Fig. 3. Migration results for a point diffractor in a constant velocity medium. Each panel displays from left to right: the final stack, the specularity gather for a given horizontal position, x, and a specularity section for given value of specularity, S. The horizontal location of the diffractor is at 1250 m. (a) x= 1250 m, S = 1.0 (b) x = 1150 m, S = 0.8.

Displaying common-image specularity gathers (vertical sections) may become cumbersome when dealing with more complicated data. Fortunately, using a common-depth display, i.e., showing sections along one of the horizontal lines (corresponding to depth in the common-image gather) versus specularity on the vertical axis is able to give a clearer image, especially for cases with small lateral variations. For these cases, in the Common-Depth Specularity Gathers (horizontal sections), the specular reflections are almost horizontal events. An important issue is that in this display one can identify (out of Fresnel zone-) ghosts of the specular events coming from deeper locations, which are also almost horizontal. In this way, we can filter these ghosts together with their primaries.

A workflow for diffraction imaging using common-depth specularity gathers consists of:

I. Standard pre-stack depth migration using formula (1) and associated migration velocity analysis to obtain an optimally focused full-wave image $V(\mathbf{x})$;

II. Extraction of the unit vector normal to the reflector surface using $V(\mathbf{x})$ in each point;

III. Migrating using eq. (3) to obtain a specularity gather;

IV. Filtering the specular energy from the specularity gather;

V. Stacking over specularity dimension to obtain a diffraction image [eq. (4)].

NUMERICAL RESULTS

The numerical results are obtained using the procedure outlined above [eqs. (1)-(4)]. The filtering step IV can be done using any procedure able to detect and attenuate laterally continuous seismic events. Here we used one of them, the Plane Wave Destruction Filter (PWD) (Fomel, 2002). Before applying the filter, we compute the dips in each section of the Common-Depth Specularity Gather. Then, in each point from the gather, the filter is performing a weighted stack along the dip in order to attenuate the seismic event from a given vertical window, if a similar event is found along the dip. The first numerical example has been designed for a proof of concept (Fig. 4) and illustrates the functionality of specularity gathers on a simple diffraction ramp model: a horizontal reflector at 900 m of depth, and a double ramp with the base at 1400 m, as depicted in the perfect migration stack shown in the panel (a) from Fig. 4. The synthetic data are generated using ray-Born approximation,

a method proved to be very useful in forward modeling diffracted waves (Moser, 2012). After pre-stack migration, the unit vector normal to the reflectors in the final stack (a) was computed and used to generate a specularity gather [eq. (3)] in a subsequent migration run. The Common-Depth Specularity

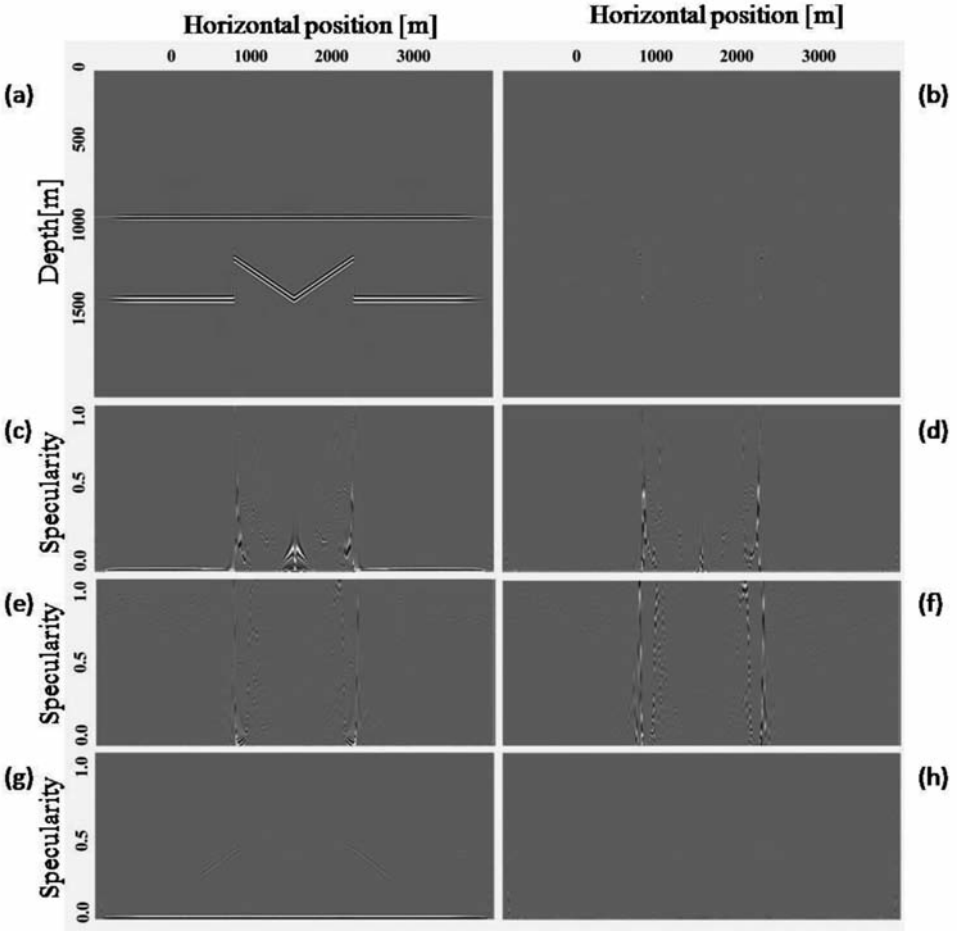

Fig. 4. Diffraction ramp model: (a) Pre-stack migration image obtained by stacking over the values of specularity in the specularity gather. (b) Diffraction image obtained by stacking over specularity of the Plane Wave Destructor (PWD) filtered specularity gather. (c) Section of the specularity gather in common-depth display for 1400 m of depth. (d) Section of the specularity gather in common-depth display filtered with PWD for 1400 m of depth. (e) Section of the specularity gather in common-depth display for 1140 m of depth. (f) Section of the specularity gather in common-depth display filtered with PWD for 1140 m of depth. (g) Section of the specularity gather in common-depth display for 900 m of depth. (h) Section of the specularity gather in common-depth display filtered with PWD for 900 m of depth.

Gather of Fig. 4c shows two horizontal events close to S = 1 coming from the specular reflections shown in the stack from Fig. 4a at 1400 m depth, while for the diffractive events from the same depth at 750 m, 1500 m, and 2250 m along the line, there are clearly defined peaks. Close to the central peak, we notice also two dipping events from the specular reflections close to the edge of the double-ramp. After applying the Plane Wave Destruction Filter the specular energy is attenuated, and the result showing three diffraction peaks is displayed in Fig. 4d. The specularity gather of Fig. 4e does not have horizontal events, but displays, close to S = 1, dipping events corresponding to the specular reflections at the top end of the ramps, visible in the stack from Fig. 4a at 1140 m in depth. For the diffractive events from the same depth at 750 m and 2250 m along the line, there are clearly defined peaks. In Fig. 4f is displayed the result of applying the Plane Wave Destruction Filter on the section from Fig. 4e: the specular energy is almost completely attenuated and two diffraction peaks are visible. The specularity gather of Fig. 4g shows a horizontal event close to S = 1 coming from the specular reflections shown in the stack from Fig. 4a at 900 m in depth, and two ghost dipping events coming from the specular reflections on the ramps. After filtering with the Plane Wave Destruction Filter, we obtain almost no energy - except for two very weak peaks at the survey's edges - as displayed in Fig. 4(h). Stacking the filtered specularity gathers over the values of specularity gives the diffraction image shown in Fig. 4(b). Almost all of the specular energy was attenuated in the final image leaving just the five points of discontinuity in the model.

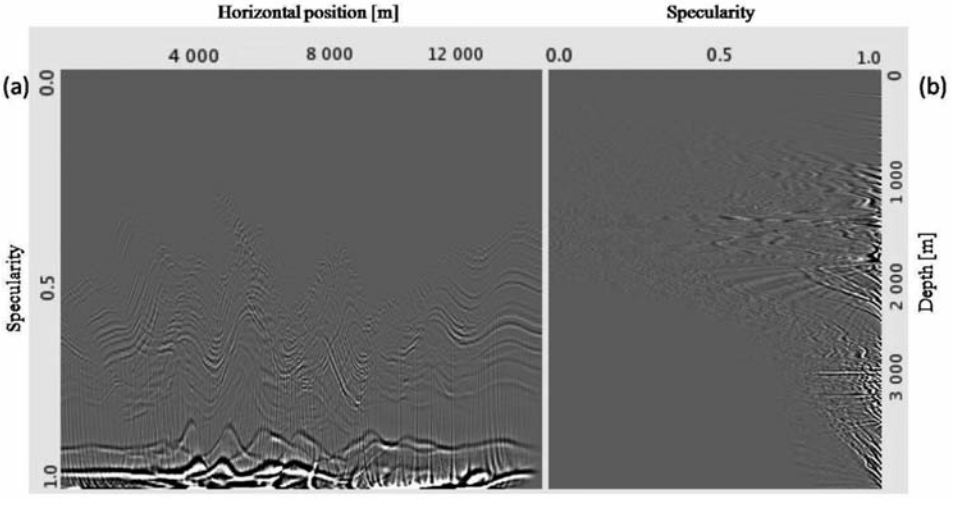

Fig. 5. Mare di Cassis model: (a) Specularity gather in common-depth display (horizontal section) for 2100 m. (b) Specularity gather in common-image display (vertical section) for the horizontal position x = 4880 m.

The second example is the Mare di Cassis data set, which is described in Moser and Howard (2008). After regular pre-stack migration, the unit vector normal to the reflectors in the final stack was computed and used to generate a specularity gather in a subsequent migration run. Fig. 5 displays a comparison between a Common Depth Specularity Gather (horizontal section) on the left, and a vertical section from the specularity gather on the right. Visually it is clear that the first one displays more information: the specular reflections are identified as laterally continuous events, the out-of-Fresnel zone ghosts are identified as similar events at smaller values of specularity, while diffractions are identified by the numerous peaks. In the vertical display the diffractions are identified by the horizontal peaks, while specular reflections by dipping events that tend to align toward the zero-specularity point from the surface. The specularity gathers were tapered along the specularity axis, and the plane wave-destructor filter was applied in the common depth sections of the gather.

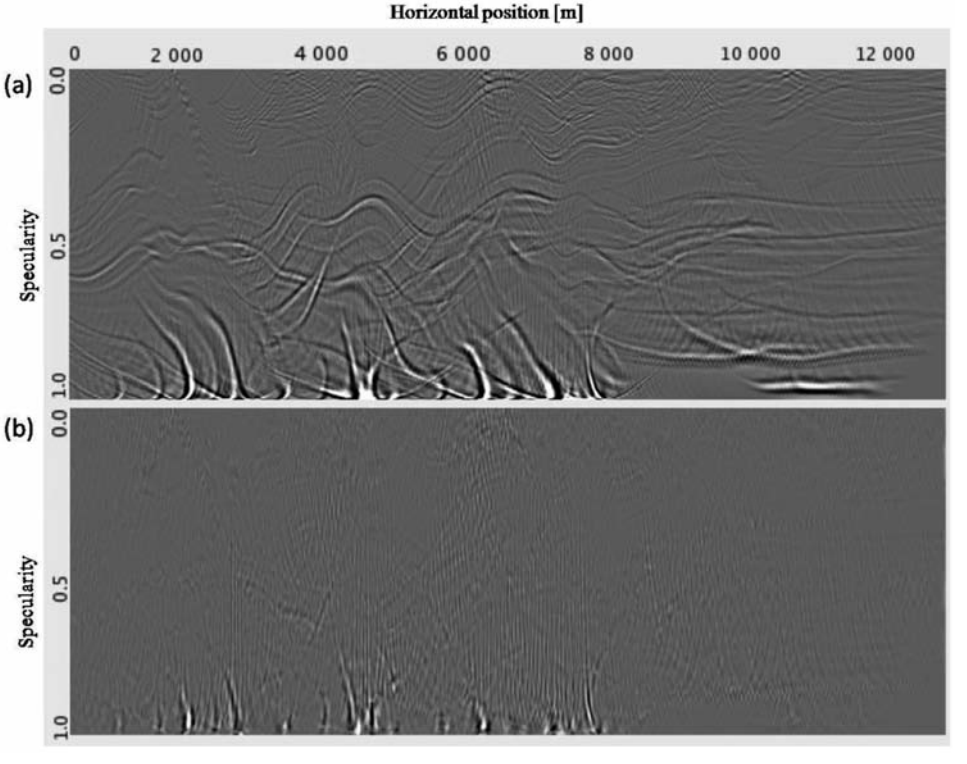

Fig. 6. Mare di Cassis model: (a) Common-Depth Specularity Gather for 1310 m. (b) PWD filtered Common-Depth Specularity Gather for 1310 m.

In Figs. 6, 7, and 8, the result of applying the plane wave-destructor filter on a common depth specularity gather is shown respectively for three values of depth. Almost all the specular energy is attenuated, except for regions close to $S=1$ where the dip calculation is affected by either multiple dips concurrently in the same image point or by vertical dips; consequently, the plane wave-destructor filter is not able to clean all the specular energy. Fig. 9 displays in panel (a) the standard migrated image, in panel (b) the diffraction image obtained by stacking over specularities smaller than 0.97 of the plane wave-destructor filtered specularity gather, and - for reference - in panel (c), the diffraction image obtained using a cubic taper to filter out all the events from the specularity gather corresponding to values of specularity larger than 0.92 (Sturzu et al., 2013). A visual comparison shows that the current procedure gives better results than that obtained using the uniform taper.

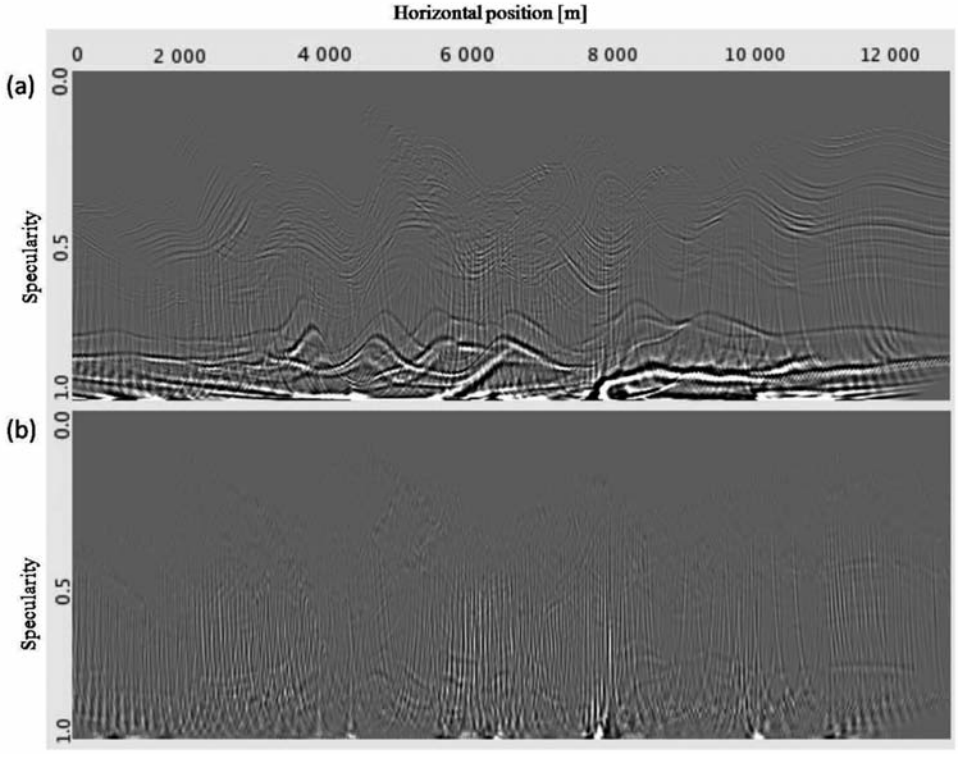

Fig. 7. Mare di Cassis model: (a) Common-Depth Specularity Gather for 1960 m. (b) PWD filtered Common-Depth Specularity Gather for 1960 m.

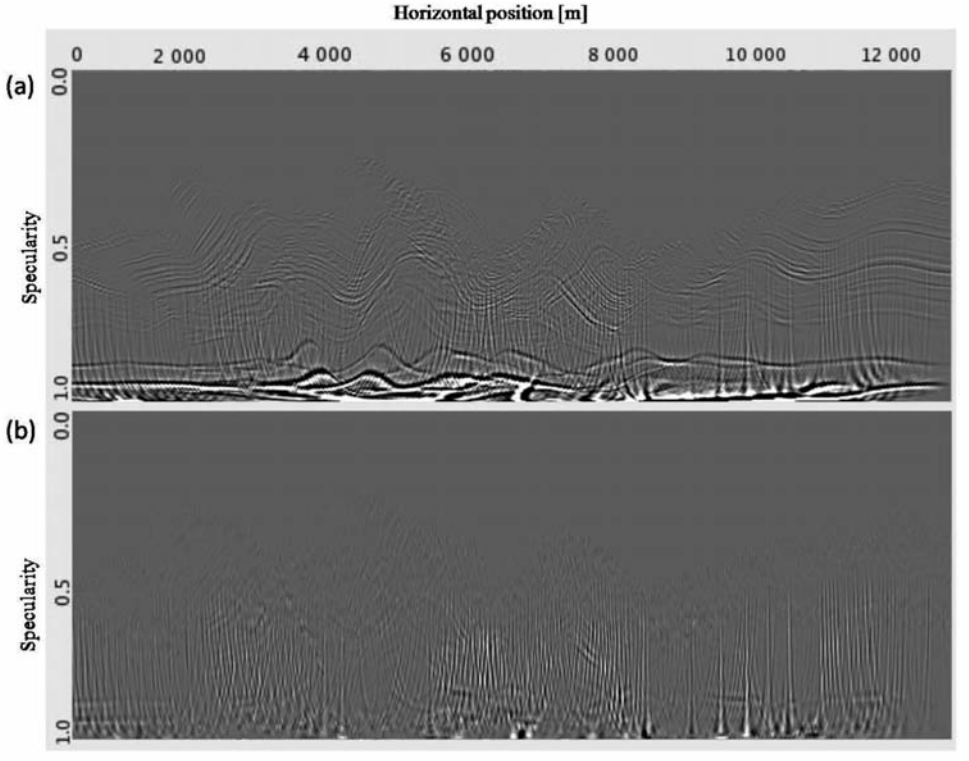

Fig. 8. Mare di Cassis model: (a) Common-Depth Specularity Gather for 2080 m. (b) PWD filtered Common-Depth Specularity Gather for 2080 m.

The third example contains a field dataset from Teapot Dome (Powder River Basin, Wyoming). Here, diffraction imaging has been carried out using the same steps as above, but in the framework of a full 3D depth imaging process. Figs. 10 and 11 show the results for a region that contains the target known as the Tensleep formation. In Fig. 10 we focus on the crossline 118 of the survey: panel (a) is the standard migration result (the top of the Tensleep formation is depicted in the figure), while panel (c) displays corresponding section from the diffraction image. The vertical section of the specularity gather at the location given by the vertical thin white line on the stack is shown in Fig. 10b, while the corresponding section from the plane wave-destructor filtered specularity gather is displayed in Fig. 10d. The filtering procedure was applied in each horizontal section (common depth specularity gather) separately, so Fig. 10d was not obtained by applying directly the plane wave-destructor in the vertical section.

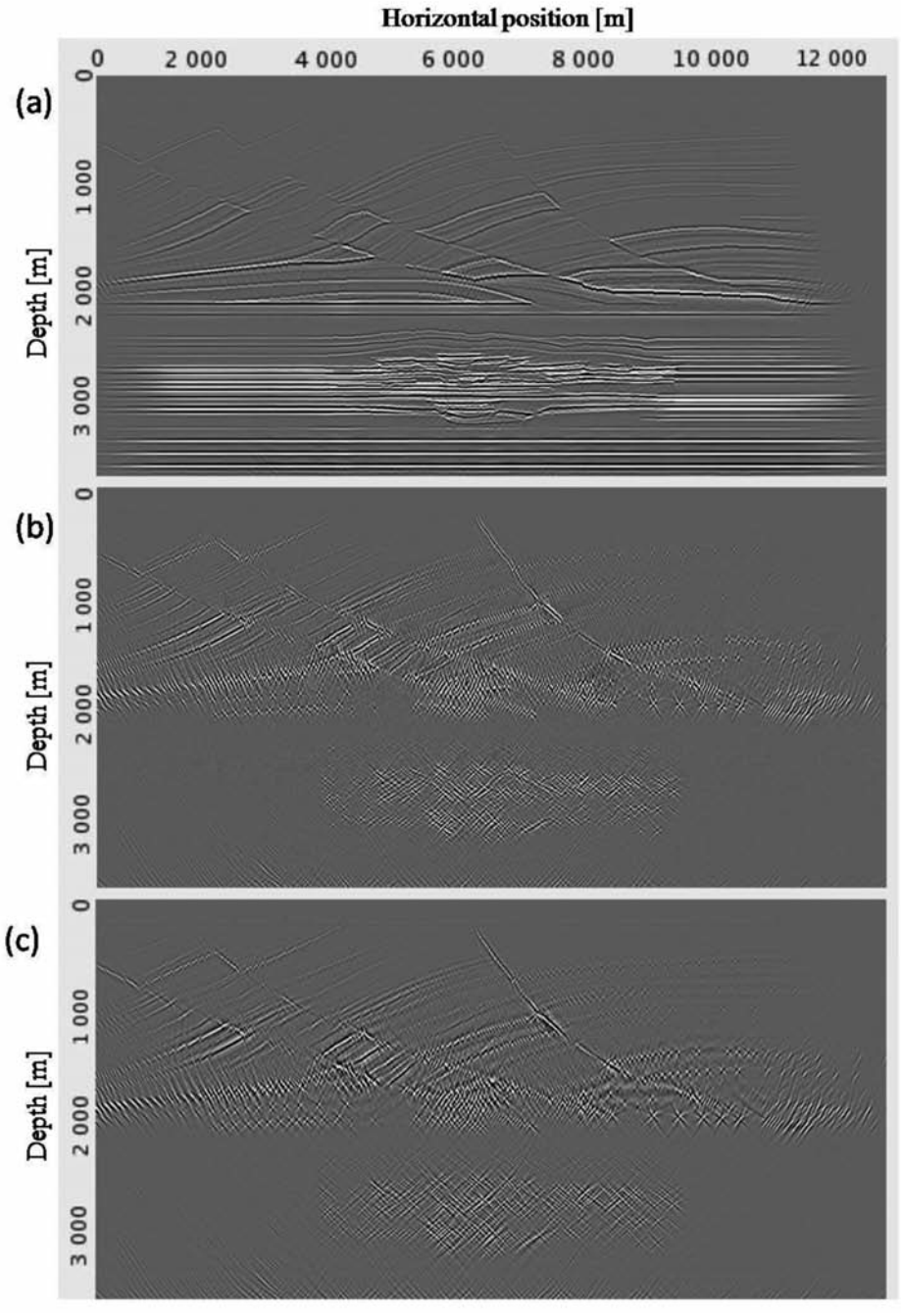

Fig. 9. Mare di Cassis model: (a) Standard migrated image; (b) Diffraction image obtained by stacking over specularity of the PWD filtered specularity gather; (c) Diffraction image obtained using a uniform taper filter above $S = 0.92$.

In Fig. 11, we focus on a depth section at 2020 m (depicted in Fig. 10a with a thin white horizontal line). Fig. 11a displays the depth section through the standard migration result, while in Fig. 11b is shown the corresponding depth section in the diffraction image. The common depth specularity gather for the crossline 118 at the same depth is shown in Fig. 11c, while the corresponding result filtered with plane wave-destructor method is depicted in Fig. 11d. In this case, due to the 3D geometry, the diffraction peaks from the specularity gather are not as clear as in the synthetic examples. However, applying the procedure described above is able to delineate in the migrated image (Fig. 11b) high-resolution diffractive elements related to the transition between different stratigraphic formations.

(a) (b)

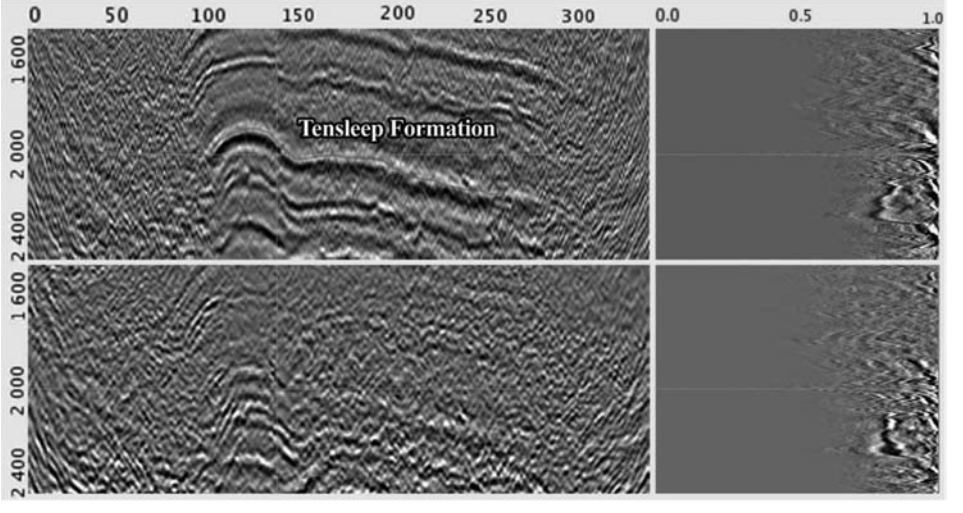

(c) (d)

Fig. 10. Teapot Dome dataset, crossline 118: (a) Standard migrated image; (b) Vertical section of the specularity gather at inline 138; (c) Diffraction image; (d) Vertical section of the specularity gather at inline 138 filtered with PWD.

CONCLUSIONS

Specularity gather analysis proves to be a very useful instrument in obtaining and/or optimizing diffraction images. The energy corresponding to higher values of specularity can be attenuated by using tapers (uniform or based on interpretation input). An automatic algorithm can be alternatively constructed by using a filter, such as plane-wave-destructor, to attenuate the specular energy at any location in the specularity gather. Further development of this method will help in advancing diffraction imaging technology.

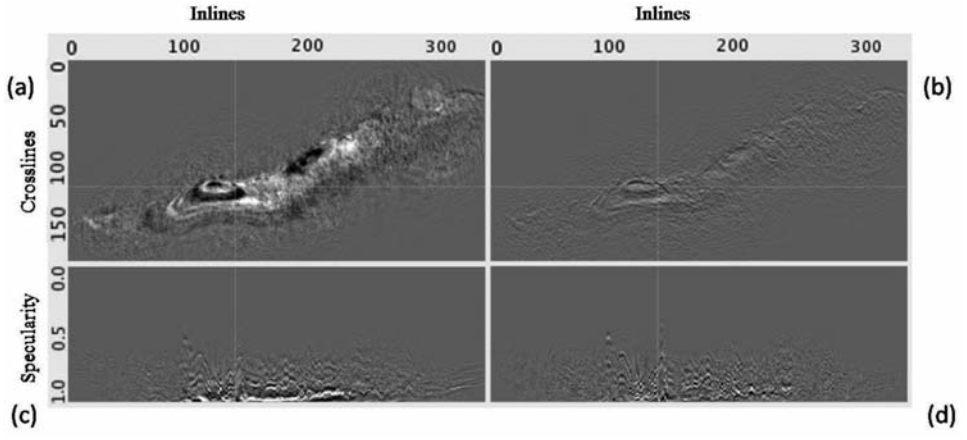

Fig. 11. Teapot Dome dataset, depth section at 2020 m: (a) Standard migrated image; (b) Diffraction image; (c) Common-Depth Specularity Gather, display at crossline 118; (d) Common-Depth Specularity Gather filtered with PWD, displayed at crossline 118.

ACKNOWLEDGEMENTS

We thank Rocky Mountain Oilfield Testing Center and the U.S. Department of Energy for providing the Teapot Dome dataset, and Opera (Pau) for providing the Mare di Cassis dataset. Special thanks are due to our anonymous reviewer, for comments that greatly improved the manuscript.

REFERENCES

Dell, S. and Gajewski, D., 2011. Common-reflection-surface-based workflow for diffraction imaging. Geophysics, 76: 187-195.

Fomel, S., Landa, E. and Taner, M.T., 2006. Post-stack velocity analysis by separation and imaging of seismic diffractions. Expanded Abstr., 76th Ann. Internat. SEG Mtg., New Orleans: 2559-2563.

Fomel, S., 2002. Applications of plane-wave destruction filters. Geophysics, 67: 1946-1960.

Khaidukov, V., Landa, E. and Moser, T.J., 2004. Diffraction imaging by focusing-defocusing: An outlook on seismic superresolution. Geophysics, 69: 1478-1490.

Klokov, A., Baina, R., Landa, E., Thore, P. and Tarrass, I., 2010. Diffraction imaging for fracture detection: synthetic case study. Expanded Abstr., 80th Ann. Internat. SEG Mtg., Denver: 3354-3358.

Klokov, A., Baina, R. and Landa, E., 2011. Point and edge diffractions in three dimensions. Extended Abstr., 73rd EAGE Conf., Vienna: B023.

Klokov, A. and Fomel, S., 2012. Separation and imaging seismic diffractions using migrated dip-angle gathers. Geophysics, 77: S131-S143.

Koren, Z. and Ravve, I., 2011. Full-azimuth subsurface angle domain wavefield decomposition and imaging, Part I: Directional and reflection image gathers. Geophysics, 76: S1-S13.

Landa, E., Fomel, S. and Reshef, M., 2008. Separation, imaging, and velocity analysis of seismic diffractions using migrated dip-angle gathers. Expanded Abstr., 78th Ann. Internat. SEG Mtg., Las Vegas: 2176-2180.

Moser, T.J. and Howard, C.B., 2008. Diffraction imaging in depth. Geophys. Prosp., 56: 627-641.

Moser, T.J., 2009. Diffraction imaging in subsalt geometries and a new look at the scope of reflectivity. Expanded Abstr., EAGE Subsalt Imaging Workshop: Focus on Azimuth, Cairo.

Moser, T.J., 2011. Edge and tip diffraction imaging in three dimensions. Extended Abstr., 73rd EAGE Conf., Vienna.

Moser, T.J., 2012. Review of ray-Born modeling for migration and diffraction modeling. Studia Geophys. Geodaet., 56: 411-432.

Shtivelman, V. and Keydar, S., 2005. Imaging shallow subsurface inhomogeneities by 3D multipath diffraction summation. First Break, 23: 39-42.

Sturzu, I., Popovici, A.M., Tanushev, N., Musat, I., Pelissier, M.A. and Moser, T.J., 2013. Specularity gathers for diffraction imaging. Extended Abstr., 75th EAGE Conf., London: We-01-03.

Taner, M.T., Fomel, S. and Landa, E., 2006. Separation and imaging of seismic diffractions using plane-wave decomposition. Expanded Abstr., 76th Ann Internat. SEG Mtg., New Orleans: 2401-2404.

Zeng, H., 2009. How thin is a thin bed? An alternative perspective. The Leading Edge, 28: 1192-1197.